ACTA PHYSICA POLONICA A No. 3 Vol. **148** (2025)

Epitaxy and Structural, Electrical, and Optical Characterization of $Pb_{1-x}Sn_xTe$ Semiconductor Layers Grown by MBE on CdTe/GaAs Hybrid Substrates

W. Wołkanowicz[a,b,*], P. Dziawa[a,b], M. Zięba[a], R. Minikayev[a],
A. Sulich[a], E. Łusakowska[a], A. Reszka[a], K. Dybko[a,b],
T. Andrearczyk[a], M. Szot[a,b], L. Kowalczyk[a], A.M. Witowski[c],
J. Polaczyński[b], W. Zaleszczyk[a], T. Wojtowicz[b] and T. Story[a,b]

[a] *Institute of Physics, Polish Academy of Sciences, al. Lotników 32/46, PL-02668 Warsaw, Poland*
[b] *International Research Centre MagTop, Institute of Physics, Polish Academy of Sciences, al. Lotników 32/46, PL-02668 Warsaw, Poland*
[c] *Faculty of Physics, University of Warsaw, Pasteura 5, PL-02093 Warsaw, Poland*

Received: 06.10.2025 & Accepted: 02.12.2025

Doi: 10.12693/APhysPolA.148.257

*e-mail: wolkanowicz@ifpan.edu.pl

$Pb_{1-x}Sn_xTe$ is a IV–VI substitutional semiconductor alloy exhibiting excellent thermoelectric and mid-infrared optoelectronic properties controlled by the tin content. In recent years, this material has gained additional interest due to discovery of a topological crystalline insulator state for large values of x. High-quality $Pb_{1-x}Sn_xTe$ crystals can be grown both as bulk materials and thin layers. However, due to its high thermal expansion and lattice mismatch with commercial semiconductor substrates such as Si or GaAs, the choice of substrates for epitaxial growth of $Pb_{1-x}Sn_xTe$ layers is very limited, and thermally matched cleaved BaF_2 (111) substrates have typically been used. In this article, we report the growth of $Pb_{1-x}Sn_xTe$ ($x = 0$–1) layers by molecular beam epitaxy using original hybrid substrates made of a few micrometer thick CdTe layer grown on commercial 2-in GaAs (001) wafers. The basic structural, electrical, and optical characteristics of the grown structures are presented, demonstrating the high crystalline quality of the $Pb_{1-x}Sn_xTe$ layers with a rock-salt structure, with a lattice parameter exhibiting Vegard law in the entire composition range, p-type electrical conductivity with hole concentration varying by three orders of magnitude from PbTe to SnTe, and a mid-infrared optical spectrum dominated by plasma reflectivity and interference effects.

topics: IV–VI semiconductors, topological crystalline insulators, epitaxial growth

1. Introduction

$Pb_{1-x}Sn_xTe$ is a IV–VI semiconductor substitutional solid solution known for its thermoelectric and mid-infrared optoelectronic applications, as well as for its intriguing electronic properties controlled through Sn content and engineering of native defects (metal vacancies) [1–3]. A recent renewed interest in this material is related to the discovery of a topological crystalline insulator (TCI) state observed for $x > 0.35$, which is driven by an inversion of the valence- and conduction-band symmetry occurring at the transition through the zero energy gap state (for $x = 0.3$–0.5 at low and room temperature, respectively), identified as a Weyl semimetal [4–8]. Successful band-structure engineering through alloying with other semiconductors, as well as achieving a very high doping level, resulted also in significant improvement in the efficiency of thermoelectric generators based on SnTe and $Pb_{1-x}Sn_xTe$ [9].

High-quality $Pb_{1-x}Sn_xTe$ crystals can be produced in bulk form using either growth from molten material by the Bridgman method, or from the vapor phase, e.g. by the self-selecting vapor growth (SSVG) technique [1–3, 10, 11]. An alternative technological approach — crucial for infrared detectors in the form of layered heterostructures — is the growth of micrometer- or nanometer-thick layers on suitable single-crystal substrates. Typically, a thermally matched, cleaved BaF_2 (111) substrates (lattice parameter $a = 6.20$ Å, thermal expansion coefficient $\alpha = 1.88 \times 10^{-5}$ K^{-1}) are

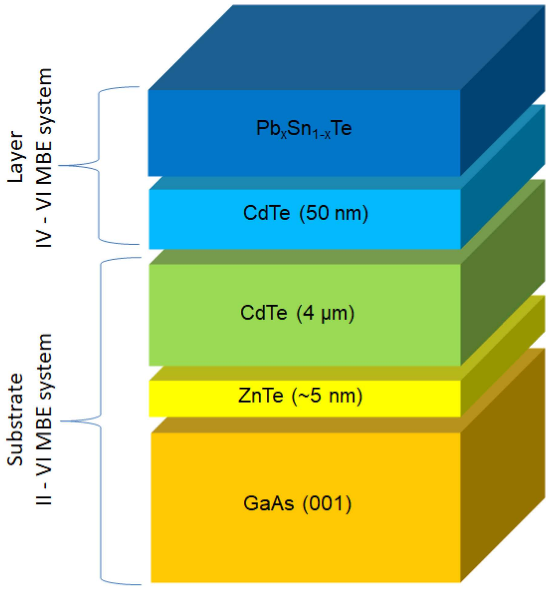

Fig. 1. Schematic diagram of the heterostructures studied in this work, consisting of a CdTe/ZnTe/GaAs (001) hybrid substrate and a Pb$_{1-x}$Sn$_x$Te ($x = 0$–1) epitaxial layer with a thickness of 0.6–3 micrometers.

used for epitaxial growth of IV–VI semiconductors. Other options studied are: KCl, InP, or IV–VI native substrates. However, KCl with lattice parameter $a = 6.29$ Å and very large thermal expansion coefficient $\alpha = 3.9 \times 10^{-5}$ K^{-1} is an exotic solution, e.g. for studies of compressive strain-induced effects. This substrate has many disadvantages, such as cracking of the layers during thermal cycling. Being a commercially available epi-ready InP substrate ($a = 5.87$ Å, $\alpha = 4.6 \times 10^{-6}$ K^{-1}) shows a small lattice parameter mismatch to PbS ($a = 5.94$ Å), a larger one to PbSe ($a = 6.12$ Å) and quite a large one to SnTe ($a = 6.30$–6.32 Å, depending on stoichiometry) and PbTe ($a = 6.46$ Å). Like other III–V semiconductors, InP also shows a large thermal expansion mismatch to IV–VI semiconductors, which typically have $\alpha \approx 2 \times 10^{-5}$ K^{-1}).

Despite quite high quality of crystals (typically 300 arcsec rocking curve parameter), IV–VI crystals never reached the status of truly commercial substrates and were, and still are, considered as a special research-oriented option or special applications of infrared p–n junction lasers. The primary reasons are: (i) the relatively small size (1 cm) of single-crystalline plates obtained, (ii) the lack of a simple and reliable mechano–chemical polishing procedure to prepare epi-ready surface of these rather soft telluride materials, and (iii) the practically unavoidable high concentration of electrically active native defects, resulting in high conductivity and metallic-like properties. The lack of semi-insulating IV–VI substrates constitutes a considerable disadvantage in developing many applications.

Due to the high thermal expansion and crystal lattice parameter mismatch of IV–VI semiconductors with commercial semiconductor substrates such as Si, GaAs or, InP, the choice of substrates for epitaxial growth of Pb$_{1-x}$Sn$_x$Te is very limited. Therefore, the development of epitaxial growth technology for IV–VI semiconductors on substrates that do not have disadvantages of cleaved BaF$_2$ substrates, associated with their limited surface area and the presence of unavoidable crystalline steps, is a timely and important research task.

In this paper, we report on molecular beam epitaxial (MBE) growth of Pb$_{1-x}$Sn$_x$Te ($x = 0$–1) layers employing original hybrid substrates made of thick CdTe layer epitaxially grown on commercial 2-in GaAs (001) wafers.

The basic structural properties as well as electrical and optical characteristics are presented, demonstrating high crystalline quality of the grown Pb$_{1-x}$Sn$_x$Te layers with a rock-salt structure across the entire composition range. These results therefore prove that the CdTe/GaAs (001) hybrid substrates are a versatile platform for developing epitaxial growth procedures not only for (001)-oriented Pb$_{1-x}$Sn$_x$Te single-crystal layers but also for various multilayer infrared or thermoelectric heterostructures.

2. Epitaxial growth and structural characterization

Pb$_{1-x}$Sn$_x$Te ($x = 0$–1) layers with a cubic rock-salt structure, studied in this work, were grown by the MBE method on a CdTe/GaAs hybrid substrates with (001) orientation and a cubic zinc-blende structure. We applied a two-step technological procedure involving two separate ultra-high vacuum (UHV) MBE systems. First, the hybrid CdTe/GaAs substrate was produced in the MBE system having a growth chamber dedicated to II–VI semiconductors. For this purpose, low-temperature effusion cells filled with $7N$ purity elemental Cd, Te, and Zn were used. Zinc-blende CdTe layers with a thickness of at least 4 micrometers, oriented in (001) direction, were epitaxially grown on (001)-oriented, two-inch, epi-ready, commercial GaAs wafers (2° off). The oxide from the GaAs substrate was removed either thermally or with the use of hydrogen plasma at 200°C. Prior the growth of CdTe layer, a very thin (about 5–20 nm) ZnTe buffer layer was grown directly on the GaAs (001) wafer. This layer is intended to suppress the tendency of CdTe to nucleate in some parts of the wafer in the (111) growth orientation instead of (001). A schematic picture of the final layered structures produced and studied in this work is shown in Fig. 1. The “Substrate” section in this figure shows the layers grown in the first (II–VI) MBE system, whereas the “Layer” section presents

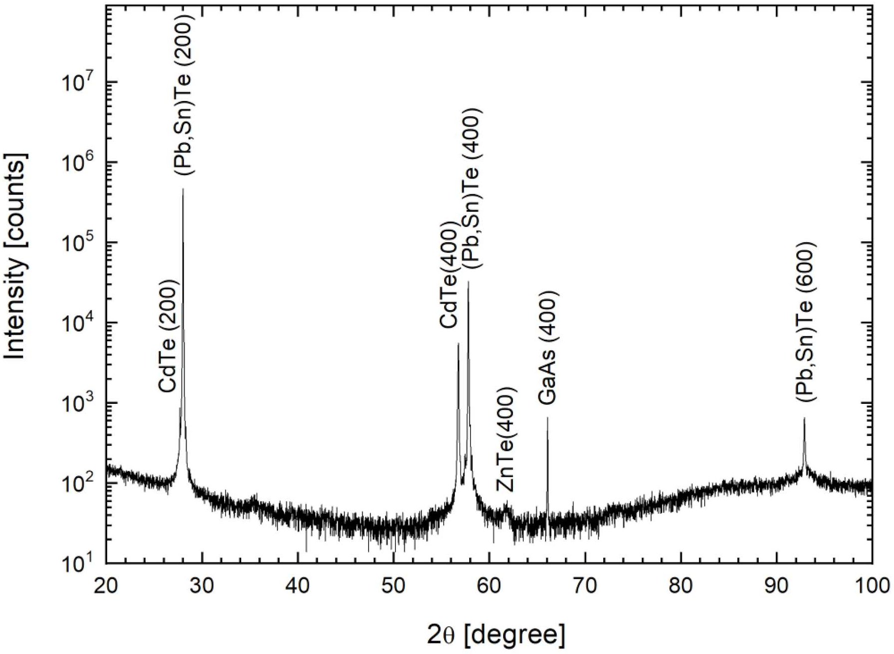

Fig. 2. X-ray 2θ–θ diffraction pattern (intensity is presented in logarithmic scale) of the $Pb_{0.48}Sn_{0.52}Te$/CdTe/GaAs heterostructure. All peaks can be assigned to (h00) Bragg peaks from the $Pb_{1-x}Sn_xTe$ layer (rock-salt type structure), the CdTe and ZnTe buffer layers, as well as the GaAs substrate (zinc-blende type structure).

the results of the technological steps carried out in the second (IV–VI) system. Just before loading (through air) the hybrid substrate to the IV–VI MBE system, the CdTe/GaAs hybrid substrate was etched in HCl and thoroughly rinsed with flowing deionized water. Growth of the $Pb_{1-x}Sn_xTe$ layer was preceded by appropriate UHV annealing of the CdTe/GaAs hybrid substrates, until a clear, streaky reflection high-energy electron diffraction (RHEED) pattern was observed from the CdTe surface. Before starting the growth of the main $Pb_{1-x}Sn_xTe$ layer (with a thickness from 0.6 to 3 microns), an additional 50 nm thick CdTe buffer layer was homoepitaxially grown on the hybrid substrate in order to provide an atomically smooth (001) surface. For the growth of $Pb_{1-x}Sn_xTe$ layer, we used a MBE chamber equipped with effusion cells filled with pieces of stoichiometry optimized polycrystalline ingot of SnTe and elemental Pb, Cd, and Te with a purity of $6N$, or higher. At each technological step carried out under UHV regime, the growth of the layers was controlled in-situ by observing a clear streaky RHEED pattern. The substrate temperature during the growth was set at $T_{\mathrm{sub}} = 270$–300°C. Typically, the additional Te flux was applied at a level corresponding to about a 10% increase of molecular flux above the stoichiometric cation-to-anion ratio. In [12] further details of the strain and surface morphology of SnTe layers of varying thickness grown by MBE method on CdTe/GaAs hybrid substrates are presented, explaining in particular the role of 2° miss cut of GaAs (001) commercial wafers used.

Compared to early attempts described in the literature [3], in which $Pb_{1-x}Sn_xTe$ layers were grown directly on GaAs (001) substrates (without any thick buffer), the strain-induced macroscopic cracking of the layers is much reduced in our layers grown on a hybrid substrate, but still occurs in some layers, as evidenced by surface morphology studies by atomic force microscopy (AFM) and scanning electron microscopy (SEM) techniques. This is particularly important in the case of charge carrier transport studies, because electrical conductivity in the layers with cracks can be two orders of magnitude lower than in the cracks-free layers.

The layers' crystal structure, lattice parameter, thickness, and chemical composition were examined by X-ray diffraction (XRD) and scanning electron microscopy (SEM), as well as energ-dispersive X-ray spectrosopy (EDX) techniques. XRD measurements were carried out in the standard 2θ–θ diffraction geometry over a broad 2θ range. An example of a typical diffraction pattern collected for a heterostructure containing 52% of tin is shown in Fig. 2. The diffraction pattern shows peaks confirming the structure and crystallographic orientation of the hybrid substrate, such as the 400 Bragg peak originating from GaAs with a cubic zinc-blende structure, as well as a low-intensity peak from the 400 planes of an ultra-thin layer of ZnTe, and the 200 and 400 peaks originating from a CdTe layer crystallized in the structure identical to that of the substrate. The $Pb_{1-x}Sn_xTe$ layer also produces peaks from the h00 planes family (200, 400, 600), but belonging

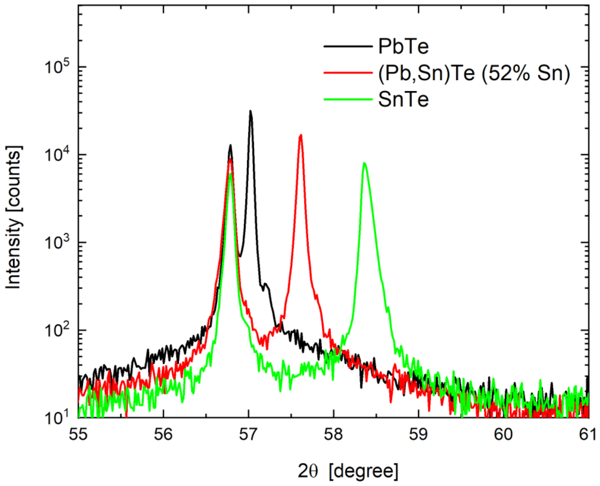

Fig. 3. X-ray diffraction patterns around the (400) Bragg peaks (intensity is presented in log scale) of $Pb_{1-x}Sn_xTe$ layers and CdTe layer. Each pattern consists of a peak due to CdTe (left) and a composition-dependent peak shifting with the change of the lattice parameter, i.e., from a larger one for PbTe (6.46 Å) to smaller one for SnTe (6.32 Å) and the corresponding smaller or larger 2θ position of the (004) reflex of $Pb_{1-x}Sn_xTe$.

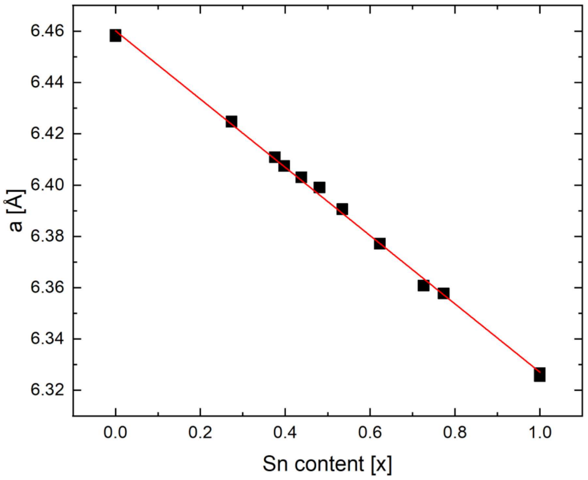

Fig. 4. Out-of-plane lattice parameter of the $Pb_{1-x}Sn_xTe$ layer as a function of Sn content. The red line shows Vegard's law for the bulk material of this solid solution, published in [3].

to a rock salt-type structure. The 2θ position of the $h00$-type Bragg peaks from this layer depends on the tin content in the solid solution. For example, the 400 peak from pure PbTe is at smaller angle compared to the position of the same peak from pure SnTe, while the peaks from $Pb_{1-x}Sn_xTe$ materials are at intermediate 2θ positions depending on the percentage of Sn (see Fig. 3). Based on the measured positions of the 400 reflections from $Pb_{1-x}Sn_xTe$, the out-of-plane lattice parameters of the $Pb_{1-x}Sn_xTe$ layers were calculated for each Sn content determined from EDX measurements. Figure 4 shows the graphical presentation of the results. The obtained values of the lattice parameters of our $Pb_{1-x}Sn_xTe$ layers with different tin contents fit a linear function. This relationship has been previously observed in bulk $Pb_{1-x}Sn_xTe$ crystals, as well as in layers grown on different substrates [1–3] and represents the well-known Vegard law for solid solutions.

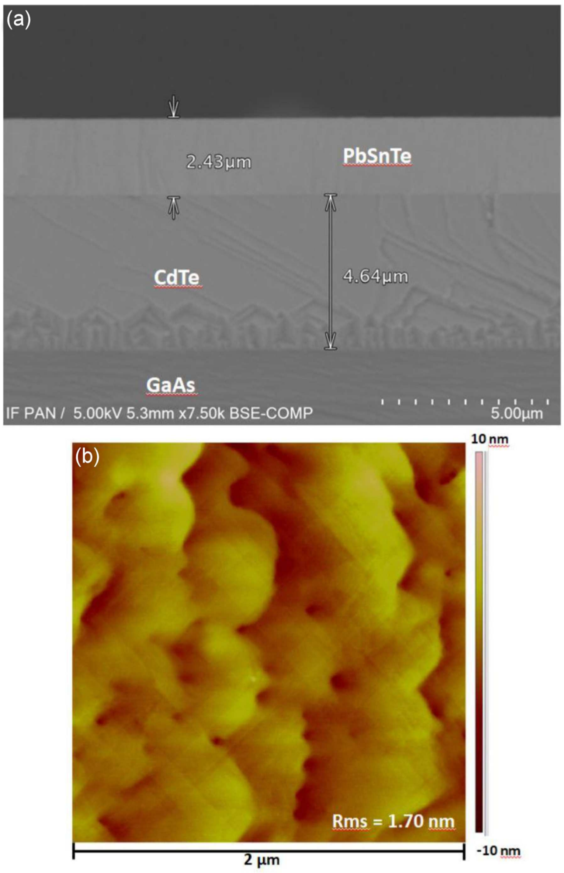

Fig. 5. SEM (a) and AFM (b) analysis of the (110) cross-section and the (001) top surface of the $Pb_{0.6}Sn_{0.4}Te$/CdTe/GaAs (001) heterostructure.

In Fig. 5 we present a SEM analysis of the (110) cross-section of PbSnTe/CdTe/GaAs heterostructure, as well as an AFM study of morphology of the (001) surface of the top layer of $Pb_{1-x}Sn_xTe$ (held in air).

3. Electronic properties

In order to characterize the electrical properties of the layers, we carried out room-temperature measurements of the Hall effect (carrier concentration) and electrical conductivity (carrier mobility). Both the semi-insulating GaAs substrates and the undoped CdTe and ZnTe layers used

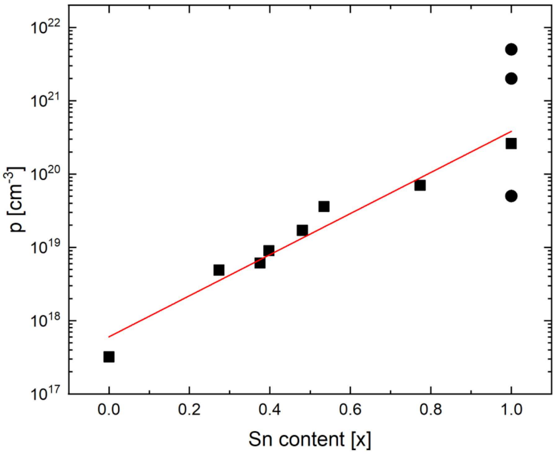

Fig. 6. Concentration of conducting holes in $Pb_{1-x}Sn_xTe$ layers as a function of Sn content (x), determined based on Hall effect measurements at room temperature. In the case of SnTe layers ($x = 1$), the effect of additional Te flux is also shown. SnTe layers were grown with different ratio of Te to SnTe flux, from 0 (the lowest hole concentration) to 0.12, 0.51, and 0.96 (the highest hole concentration). In studies of the relationship between hole concentration and tin content, an additional Te flux was set to be ≈ 0.1 of PbTe, SnTe or (Pb, Sn)Te flux (data points shown as squares). The red line is a guide for the eyes only.

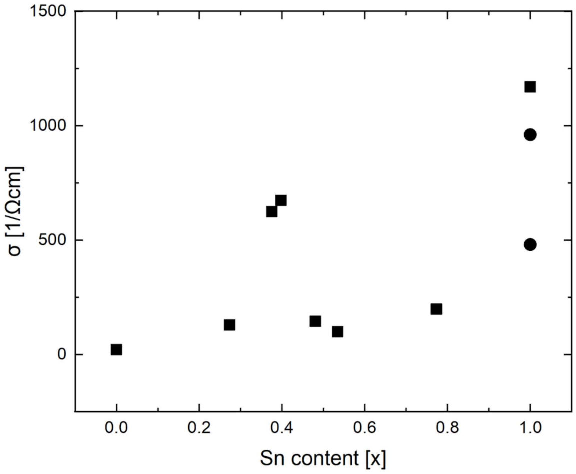

Fig. 7. Room temperature electrical conductivity of $Pb_{1-x}Sn_xTe$ layers with various Sn content (x), for which hole concentration was presented in Fig. 6. Data for SnTe are presented by two dots with additionall flux ratio of 0.51 and 0.96 as well as one square for additional Te flux ratio 0.12 (used for comparing PbSnTe layers with varying Sn content).

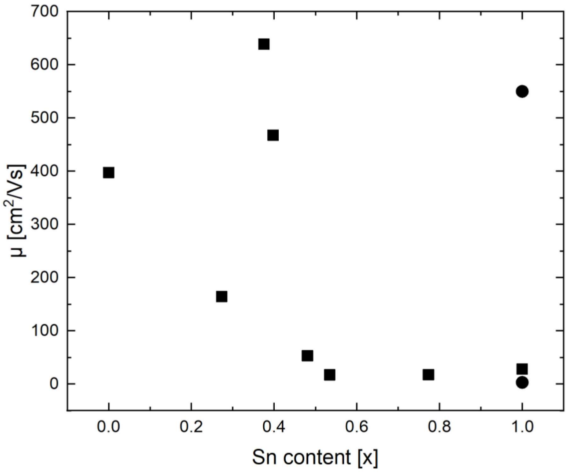

Fig. 8. Room temperature mobility of conducting holes in $Pb_{1-x}Sn_xTe$ layers with various Sn content (x). Data for SnTe are presented by two dots corresponding to flux ratio of 0.51 and 0 as well as one square for additional flux ratio of 0.12 (used for comparing PbSnTe layers with varying Sn content).

in our hybrid substrates show insulating properties and very high resistivity. Therefore, the top $Pb_{1-x}Sn_xTe$ layer we study is the only electrically conducting material in the stack. We used a four-probe DC technique with a Keithley nanovoltmeter working in delta mode and applying an electric current of $I = \pm(0.1\text{–}1)$ mA and a magnetic field of $B = \pm 0.65$ T. The electrical ohmic contacts were prepared by soldering of 50-micrometer-thick gold wires with indium. The samples in the form of Hall bars were cleaved from the wafer along the (110) crystal direction with a typical width of 2 mm and length of 8 mm.

All studied layers exhibited p-type conduction, with the hole concentration varying from $p = 3 \times 10^{17}$ cm^{-3} (in PbTe) to $p = 2 \times 10^{21}$ cm^{-3} (in SnTe) in a remarkably regular way, as shown in Fig. 6 in semi-logarithmic scale. This is the result expected for IV–VI semiconductors, in which native defects (metal vacancies) are double-acceptors with zero ionization energy (defect energy levels degenerate with band states), which induce metallic conductivity preserved down to the lowest temperatures. By varying the additional flux of Te molecules one can influence the concentration of conducting holes in SnTe ($x = 1$) by over one order of magnitude, as shown in Fig. 6. The result ($p = 5 \times 10^{21}$ cm^{-3}) for the highest non-stoichiometric ratio tested (with additional Te flux equal to that of SnTe) is not reliable because it already falls outside the stoichiometry deviation window thermodynamically possible in a single-phase crystalline SnTe material. In the case of PbTe and $Pb_{1-x}Sn_xTe$ the effect of excess Te flux is much smaller, but is still known to generate p-type conduction at the level of $p = 10^{18}\text{–}10^{19}$ cm^{-3}. The lowest carrier concentration is observed for samples grown without an additional Te flux, using only an effusion cell with SnTe polycrystalline charge, which by nature exhibit a slight non-stoichiometry (Sn deficiency — Te excess), known from the thermodynamic properties of these materials [1, 2].

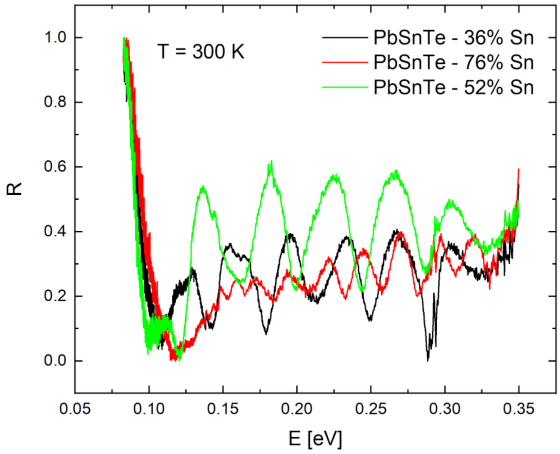

Fig. 9. Room temperature reflectivity (normalized to unity at the lowest energies) in the mid-infrared spectral range for three over 2 μm thick $Pb_{1-x}Sn_xTe$ layers, with compositions covering both the topologically trivial ($x = 0.36$) and non-trivial state ($x = 0.76$).

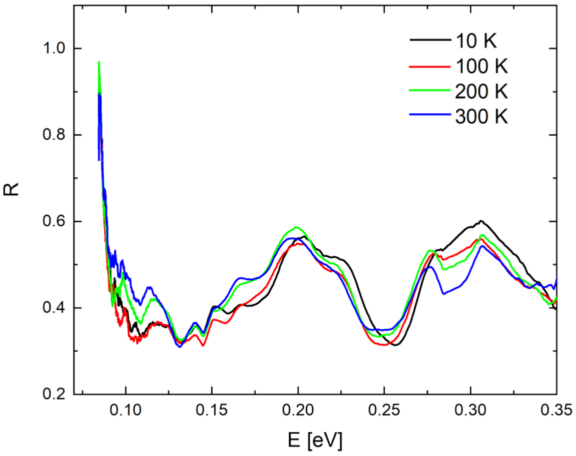

Fig. 10. Spectral dependence of reflectivity of the $Pb_{0.5}Sn_{0.5}Te$ layer collected at temperatures corresponding to both the topologically trivial band ordering ($T = 200, 300$ K) and the inverted (TCI) band ordering ($T = 10, 100$ K).

The room temperature electrical conductivity of $Pb_{1-x}Sn_xTe$ layers with varying Sn content (the same as in Fig. 6) is shown in Fig. 7, while the corresponding carrier (hole) mobility is presented in Fig. 8. We note a large scatter of the data, revealing the key influence of the non-stoichiometry regime applied during growth. One can find both layers with mobility comparable to the values observed for $Pb_{1-x}Sn_xTe$ layers grown on other, more often used substrates, such as BaF_2 (111), as well as layers with a mobility an order of magnitude lower, presumably due to the very high concentration of structural defects related to structural and thermal mismatch.

Optical studies of the layers were carried out through measurements of light reflectivity in the infrared spectral region $h\nu = 80$–350 meV (see Fig. 9). A continuous-flow cryostat with a ZnSe window and an HgCdTe photodiode detector were used. In order to account for absorption in air, we collected the reference spectrum of reflection from an Au metallic mirror immediately before measuring the reflectivity from the layer and used it in the data analysis. The photon energy range that was used covers the important energy scales in $Pb_{1-x}Sn_xTe$ material, namely the energy gap E_G for direct electronic transitions, and the plasma edge energy of 100–200 meV, expected for $Pb_{1-x}Sn_xTe$ layers with hole concentration of $p = 10^{19}$–10^{20} cm^{-3} [1–3]. The energy gap of $Pb_{1-x}Sn_xTe$ is changing with Sn content in a continuous way from $E_G = +300$ meV in PbTe to $E_G = -200$ meV in SnTe (room temperature values) with zero gap state $E_G = 0$ at the band inversion point [1–3]. For the $Pb_{0.5}Sn_{0.5}Te$ layer with a thickness of 0.825 μm we also measured reflectivity as a function of temperature from 10 to 300 K (see Fig. 10). This range includes the temperature at which the zero energy gap state occurs ($T \approx 120$ K), as well as higher temperatures at which the topologically trivial state exist, and lower temperatures where $Pb_{1-x}Sn_xTe$ assumes the topological state.

4. Discussion

Since early attempts to epitaxially grow $Pb_{1-x}Sn_xTe$ layers directly on GaAs substrates turned out unsuccessful [3], the concept of reducing the mismatch by using a very thick CdTe buffer layer with an additional thin intermediate ZnTe layer was tested in just few papers, only for SnTe [12–18]. The structural parameters of our layers compare favorably with these data. All the $Pb_{1-x}Sn_xTe$ epitaxial layers crystallize in a cubic rock-salt structure with the (001) growth direction. This is expected for IV–VI semiconductors, in which (001) facets spontaneously develop during the growth of bulk single-crystals or nanowires. No evidence for rhombohedral distortion along the (111) direction was found. We note that in the $Pb_{1-x}Sn_xTe$/CdTe heterostructure we have two cubic materials, but crystallizing in different crystal structures, i.e., in rock-salt and zinc-blende, respectively. One observes an almost ideal matching of the lattice parameters of CdTe to PbTe, but nearly 3% lattice mismatch to SnTe. This influences the crystalline order at the interface and the encountered crystal strain regime. In both cases, a strong thermal mismatch is present. Namely, at room temperature the thermal expansion coefficient for $Pb_{1-x}Sn_xTe$ is approximately $\alpha = (2.0$–$2.1) \times 10^{-5}$ K^{-1}, while for CdTe and GaAs is significantly smaller, i.e, $\alpha = 4.7 \times 10^{-6}$ K^{-1} and $\alpha = 5.9 \times 10^{-6}$ K^{-1}, respectively.

Electrical characterization of the layers based on the Hall effect and conductivity measurements at room temperature revealed p-type electrical conductivity, with the hole concentration varying by three orders of magnitude from PbTe to SnTe, and showing a regular trend as a function of composition. The actual parameters are strongly dependent on the stoichiometric regime used during growth, controlled by an additional (from 10 to 100%) Te flux. However, due to the large structural and thermal mismatch between the $\mathrm{Pb}_{1-x}\mathrm{Sn}_x\mathrm{Te}$ layers and hybrid substrates, the observed conductivity and carrier mobility values are, at best, about half of the peak values reported for reference bulk materials or thick layers grown on BaF_2 (111) substrates. In many layers, strain-induced cracks can be encountered, which obscure electrical measurements and require the use of sub-millimeter or even sub-micrometer structures in the Hall-bar geometry [15–18]. The high electrical conductivity and carrier mobility observed for the $\mathrm{Pb}_{1-x}\mathrm{Sn}_x\mathrm{Te}$ alloy with Sn content of about $x \approx 0.4$ have the same physical origin. At the same composition, $\mathrm{Pb}_{1-x}\mathrm{Sn}_x\mathrm{Te}$ is very close to be in the zero-gap state, which, after accounting for the effect of lattice distortion on valley degenerate band states, is known to correspond to a Weyl semimetal state with linear energy dispersion and very small effective mass of carriers, i.e., large mobility (see [7, 8]). We underline, however, that although this is the most likely explanation, the electrical properties of $\mathrm{Pb}_{1-x}\mathrm{Sn}_x\mathrm{Te}$ strongly depend on the concentration of metal vacancies (native acceptor centers) and possible compensation mechanism by the native donors (interstitials or Te-sublattice vacancies) — both depending on non-stoichiometry (Te to (Pb, Sn) flux ratio) and controlled by growth conditions or thermal annealing.

The observed spectral dependence of the reflectivity of the layers across the entire temperature range studied is dominated by the effect of bulk plasma reflectivity, modulated by the interference effect in the thin layer. It is seen that high reflectivity at 80 meV is followed by a plasma minimum and saturates at about 40% of reflectivity above the plasma frequency but below the absorption edge for interband transitions E_a). The high reflectivity is associated with a specific feature of IV–VI materials, which are known for their exceptionally high ($n = 6$–7) refractive index related to the structural transition and the paraelectric or even ferroelectric state observed in materials with high tin content [2, 3]. We note that due to the high hole concentration, resulting in the Fermi energy of about 100 meV and more, we expect a very strong Burnstein–Moss shift of the absorption edge for direct optical transitions determined as $E_a = E_G + E_{\mathrm{FV}} + E_C(k_{\mathrm{F}})$, where E_{FV} is the Fermi energy in the valence band, k_{F} is the Fermi wavevector, and $E_C(k_{\mathrm{F}})$ is the energy of an electron in the conduction band for $k = k_{\mathrm{F}}$. We note that these two energy terms are practically the same in the case of a semiconductor with almost mirror-symmetric bands, such as those encountered in $\mathrm{Pb}_{1-x}\mathrm{Sn}_x\mathrm{Te}$. This problem was noticed already in early reflectivity studies of closely related bulk TCI crystals of $\mathrm{Pb}_{1-x}\mathrm{Sn}_x\mathrm{Se}$ [19–21]. In narrow gap semiconductors, like $\mathrm{Pb}_{1-x}\mathrm{Sn}_x\mathrm{Te}$, with carrier effective mass and density of states depending on the band gap, an interplay between the small energy gap but the large Fermi energy results in a rather weak dependence of the optical properties on the Sn content and the band inversion point. Therefore, our reflectivity measurements showed no sharp differences between the spectra of $\mathrm{Pb}_{0.5}\mathrm{Sn}_{0.5}\mathrm{Te}$ layer collected across the inversion point (realized by temperature control), nor for the spectra collected for $\mathrm{Pb}_{1-x}\mathrm{Sn}_x\mathrm{Te}$ layers with compositions corresponding to topologically trivial and nontrivial electronic structure.

5. Conclusions

In summary, we reported successful MBE growth of $\mathrm{Pb}_{1-x}\mathrm{Sn}_x\mathrm{Te}$ (001) epitaxial layers in the full composition range ($x = 0$–1) using hybrid substrates made of GaAs (001) wafer, with a couple of microns-thick MBE grown CdTe (001) layer. Electrical characterization of the layers based on the Hall effect and conductivity measurements revealed p-type electrical conductivity, with the hole concentration varying by over three orders of magnitude from PbTe to SnTe. The actual electric parameters strongly depend on the stoichiometry regime applied during the growth, controlled by an additional Te flux. Due to large structural and thermal mismatch between the $\mathrm{Pb}_{1-x}\mathrm{Sn}_x\mathrm{Te}$ layer and the hybrid substrates, the observed conductivity and carrier mobility values are, at best, about half of the highest values reported for these materials in the bulk form.

Optical studies in the mid-infrared range revealed that the reflectivity is dominated by the plasma reflectivity and interference effects in thin $\mathrm{Pb}_{1-x}\mathrm{Sn}_x\mathrm{Te}$ layers characterized by a very high refractive index. No clear difference was found in the reflectivity spectra for $\mathrm{Pb}_{1-x}\mathrm{Sn}_x\mathrm{Te}$ layers with Sn content corresponding to topologically trivial and nontrivial (TCI) electronic structure.

Acknowledgments

This study has been supported by the Foundation for Polish Science project “MagTop” No. FENG.02.01-IP.05-0028/23 co-financed by the European Union from the funds of Priority 2 of the European Funds for a Smart Economy Program 2021–2027 (FENG) and by the National Science Centre for Development

(Poland) through grant TERMOD No. TECHMATSTRATEG2/408569/5/NCBR/2019. The polycrystalline, stoichiometry optimized SnTe binary compound used in this study as a source material for the effusion cell was prepared in the Institute of Physics Polish Academy of Sciences by J. Korczak.

References

[1] Yu.I. Ravich, B.A. Efimova, I.A. Smirnov, *Semiconducting Lead Chalcogenides*, Ed. L. Stil'bans, Springer, New York 1970.

[2] G. Nimtz, B. Schlicht, in: *Narrow-Gap Semiconductors*, Vol. 98, Springer, Berlin, Heidelberg 1983, p. 1.

[3] G. Springholz, in: *Lead Chalcogenides Physics and Applications*, Ed. D.R. Khokhlov, Taylor and Francis Books, New York 2003.

[4] P. Dziawa, B.J. Kowalski, K. Dybko et al., *Nat. Mater.* **11**, 1023 (2012).

[5] Y. Tanaka, Z. Ren, T. Sato, K. Nakayama, S. Souma, T. Takahashi, K. Segawa, Y. Ando, *Nat. Phys.* **8**, 800 (2012).

[6] S.-Y. Xu, C. Liu, N. Alidoust et al., *Nat. Commun.* **3**, 1192 (2012).

[7] A. Łusakowski, P. Bogusławski, T. Story, *Phys. Rev. B* **98**, 125203 (2018).

[8] Z. Wang, Q. Liu, J.-W. Luo, A. Zunger, *Mater. Horiz.* **6**, 2124 (2019).

[9] X.J. Tan, H.Z. Shao, J. He, G.Q. Liu, J.T. Xu, J. Jiong, H.C. Jiang, *Phys. Chem. Chem. Phys.* **18**, 7141 (2016).

[10] A. Szczerbakow, K. Durose, *Prog. Cryst. Growth Charact. Mater.* **51**, 81 (2005).

[11] A. Szczerbakow, H. Berger, *J. Cryst. Growth* **139**, 172 (1994).

[12] A. Sulich, E. Łusakowska, W. Wołkanowicz, P. Dziawa, J. Sadowski, B. Taliashvili, T. Wojtowicz, T. Story, J.Z. Domagała, *J. Mater. Chem. C* **10**, 3139 (2024).

[13] R. Ishikawa, T. Yamaguchi, Y. Ohtaki, R. Akiyama, S. Kuroda, *J. Cryst. Growth* **453**, 124 (2016).

[14] M. Kobayashi, S. Nan, *J. Cryst. Growth* **628**, 127531 (2024).

[15] D. Śnieżek, J. Wróbel, M. Kojdecki, C. Śliwa, S. Schreyeck, K. Brunner, L.W. Molenkamp, G. Karczewski, J. Wróbel, *Phys. Rev. B* **107**, 045103 (2023).

[16] D. Śnieżek, C. Śliwa, K. Dybko, J. Wróbel, P. Dziawa, T. Wojtowicz, T. Story, J. Wróbel, arXiv:2503.07039 (2025).

[17] P. Sidorczak, W. Wołkanowicz, A. Kaleta et al., arXiv:2406.04447 (2024).

[18] J.M. Głuch, M. Szot, S. Chusnutdinow, G. Karczewski, *Appl. Phys. Lett.* **126**, 121101 (2025).

[19] M. Woźny, W. Szuszkiewicz, M. Dyksik, M. Motyka, A. Szczerbakow, W. Bardyszewski, T. Story, J. Cebulski, *New J. Phys.* **26**, 063008 (2024).

[20] A.A. Reijnders, J. Hamilton, V. Britto, J.-B. Brubach, P. Roy, Q.D. Gibson, R.J. Cava, K.S. Burch, *Phys. Rev. B* **90**, 235144 (2014).

[21] N. Anand, S. Buvaev, A.F. Hebard, D.B. Tanner, Z. Chen, Z. LI, K. Choudhary, A.B. Sinnott, G. Guo, C. Martin, *Phys. Rev. B* **90**, 235143 (2014).